Nickel Carbide as a Source of Grain Rotation in Epitaxial Graphene

Peter Jacobson,[†,‡,*] Bernhard Stöger,[‡] Andreas Garhofer,[‡,#] Gareth S. Parkinson,[‡] Michael Schmid,[‡] Roman Caudillo,[§] Florian Mittendorfer,[‡,#] Josef Redinger,[‡,#] and Ulrike Diebold[‡,*]

[†]Department of Physics, Tulane University, New Orleans, Louisiana 70118, United States, [‡]Institute of Applied Physics, and [#]Center for Computational Materials Science Vienna University of Technology, Vienna, Austria, and [§]Intel Corporation, Components Research, 2501 NW 229th Avenue, RA3-252, Hillsboro, Oregon 97124, United States

ABSTRACT

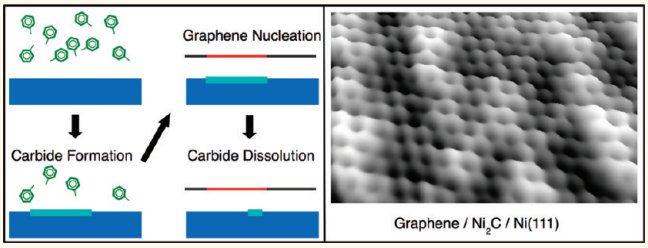

Graphene has a close lattice match to the Ni(111) surface, resulting in a preference for 1 × 1 configurations. We have investigated graphene grown by chemical vapor deposition (CVD) on the nickel carbide (Ni_2C) reconstruction of Ni(111) with scanning tunneling microscopy (STM). The presence of excess carbon, in the form of Ni_2C, prevents graphene from adopting the preferred 1 × 1 configuration and leads to grain rotation. STM measurements show that residual Ni_2C domains are present under rotated graphene. Nickel vacancy islands are observed at the periphery of rotated grains and indicate Ni_2C dissolution after graphene growth. Density functional theory (DFT) calculations predict a very weak (van der Waals type) interaction of graphene with the underlying Ni_2C, which should facilitate a phase separation of the carbide into metal-supported graphene. These results demonstrate that surface phases such as Ni_2C can play a major role in the quality of epitaxial graphene.

KEYWORDS: chemical vapor deposition · polycrystalline graphene · STM · DFT · grain boundary · nickel

Graphene, with its exemplary electronic and mechanical properties, has thoroughly infiltrated the worlds of chemistry, materials science, and physics.[1] Initially investigated for its electronic properties, graphene and its derivatives (and composites) are now widely studied for uses beyond solid-state physics.[2,3] To date, mechanical exfoliation and epitaxial growth have been the predominant sources of graphene for proof-of-concept devices. While mechanically exfoliated graphene has excellent electronic properties, it is not scalable. Silicon carbide (SiC) has been widely used to grow monolayer and few-layer graphene of very high quality with the advantage that the graphene resides on a wide band gap semiconductor.[4,5] While graphene on SiC is advantageous for many electronic applications, a major drawback is the inability to remove graphene from the SiC substrate. Graphene grown by chemical vapor deposition (CVD) on transition metals represents an alternative method of producing high-quality graphene with the advantage that the graphene can be removed by chemical etching of the underlying metal substrate.[6,7] CVD-grown epitaxial graphene has been investigated on numerous transition metals[8] (*e.g.*, Ru, Pt, Ir, Rh, Co, Ni, and Cu) and alloys (*e.g.*, Au–Ni,[9] Cu–Ni,[10,11] Ni–Mo[12]), but applied research has largely focused on utilizing Ni and Cu substrates.

While rapid advances in controlling the CVD growth process have been made, graphene formed by this method is polycrystalline. Characterization of polycrystalline graphene using transmission electron microscopy (TEM) has revealed graphene grain boundaries and determined statistical distributions of grain rotation and size.[13,14] Yu *et al.* were able to appreciably increase the size of single-crystalline graphene islands—thereby reducing the density of grain boundaries—on Cu by lithographically creating graphene seeds, but grain orientation could not be controlled.[15] The difficulty in controlling grain orientation on Cu can be attributed to the lack of a preferred epitaxial relationship, in clear contrast to Ni surfaces.[16]

Epitaxial graphene on Ni(111) represents a straightforward model system to investigate surface structures introduced during the CVD growth process. Graphene on Ni(111) adsorbs in one of several 1 × 1 structures due to a small lattice mismatch of 1.3% with the substrate, and each graphene sublattice (A and B) is situated on a different adsorption site (*i.e.*, top, fcc, hcp, bridge). The energetic difference between these structures is small, and they have recently been shown to coexist.[17] In addition to these 1 × 1

* Address correspondence to jacobson@iap.tuwien.ac.at, diebold@iap.tuwien.ac.at.

Received for review February 10, 2012 and accepted March 13, 2012.

Published online March 13, 2012
10.1021/nn300625y

structures, several local moiré structures have been observed on Ni(111).[18−21] While the coexistence of different 1 × 1 configurations is not unexpected, it is unclear why moiré structures should be observed. Given the overwhelming preference for 1 × 1 configurations, it should be possible to identify the sources of grain rotation in graphene on Ni(111).

We have used scanning tunneling microscopy (STM) and density functional theory (DFT) calculations to investigate defect structures formed during the CVD growth of graphene on Ni(111). Local regions with excess carbon in the form of the surface-confined nickel carbide (Ni_2C) prevent graphene from adopting its preferred 1 × 1 epitaxial relationship on Ni(111). Graphene has no epitaxial relationship with the carbide reconstruction, resulting in a range of grain rotations—from 6.6 to 23.8°.

RESULTS

When Ni(111) is exposed to hydrocarbons above 300 °C, the surface reconstructs into a monolayer surface carbide with stoichiometry Ni_2C (Figure 1a, model from DFT).[22−24] Figure 1b shows a large-scale image of the carbon-induced reconstruction on Ni(111). A range of domain sizes and orientations are observed with the surface possessing greater than 90% Ni_2C coverage. In images larger than ∼20 × 20 nm^2, the dominant features indicating the presence of nickel carbide are parallel lines with a spacing of 1.65 nm and an apparent height modulation of 20 pm (Figure 1b, yellow lines).

Atomic carbon strongly chemisorbs on Ni(111), penetrating the topmost layer and becoming nearly coplanar with nickel. As the carbon forces itself into the top nickel layer, the nickel−nickel distance is increased ∼3% and the local structure is distorted, effectively changing the hexagonal symmetry of the (111) surface into a square mesh similar to the (100) face (Figure 1a). This reconstruction includes clockwise and counterclockwise rotations of the square carbon lattice; hence, this surface carbide is known as the "clock reconstruction". The distortion to a square lattice on a hexagonal surface results in an incommensurate surface overlayer which can be approximated as a ($\sqrt{39}R16.1° \times \sqrt{37}R$-34.7°) structure (Figure 1a).[22] In our DFT calculations, this structure has almost the same surface energy (less than 0.01 eV/$Å^2$ difference) as the formerly proposed ($\sqrt{39}R16.1° \times \sqrt{39}R$-16.1°) structure.[24] The notation indicates the carbide unit cell orientation with respect to the Ni(111) unit cell; specifically, rotations of 16.1 and −34.7° from the [1−10] direction and with 110.8° between basis vectors. Figure 1c shows the local structure of Ni_2C by STM; on this surface, carbon is imaged as a depression (black dots denote carbon). The parallel lines seen in large-scale images (Figure 1b) are marked with yellow lines. Figure 1d shows the fast Fourier transform (FFT) of the Ni_2C domain in Figure 1c. The Fourier spots of the underlying hexagonal Ni(111) surface are circled in black in Figure 1d. The carbon lattice and the clock-work unit cell are very nearly square, as determined by Klink *et al.*,[22] and show periodicities of 3.6 Å (Figure 1d, blue circles) and 5.2 Å (Figure 1d, purple circles), respectively. The stripes observed in large-scale images (Figure 1b) are also present in the FFT and indicate a periodicity of 16.5 Å. These characteristic features allow Ni_2C to be readily identified, in effect acting as a fingerprint for the presence of Ni_2C. Figure 1e contains a simulated STM image of the ($\sqrt{39}R16.1° \times \sqrt{37}R$-34.7°) Ni_2C reconstruction overlaid with the top view model. This simulation reproduces the experimentally observed square structure in Figure 1c.

Figure 2a shows graphene grown on the Ni_2C-covered Ni(111) surface presented in Figure 1b. At the center of Figure 2a, we observe a roughly triangular area containing a labyrinth of lines that join at 120°, reflecting the underlying symmetry of the graphene monolayer and the clean nickel surface. A color-coded map of Figure 2a is shown in Figure 2b to assist identification of the distinct regions. The central triangular region (yellow) in Figure 2b contains a moiré pattern and is bound by 1 × 1 graphene and graphene on Ni_2C (Figure 2b, red and blue, respectively). The interface between the 1 × 1 graphene (red) and moiré-patterned graphene (yellow) is a tilt grain boundary. The graphene grain is continuous (no grain boundary) across the interface between moiré-patterned graphene (yellow) and graphene on Ni_2C (blue), and the difference between these regions is the presence of a Ni_2C domain underneath a portion of the graphene sheet; this will be shown more fully in what follows.

Figure 2c shows a high-resolution image of the boundary between the moiré-patterned graphene and graphene on Ni_2C, as indicated by the black box in Figure 2a. The upper half of Figure 2c contains a moiré pattern indicating rotation of the graphene sheet away from the expected 1 × 1 binding sites. Taking the FFT of the upper half of Figure 2c, we observe primary hexagonal spots corresponding to the 2.49 Å periodicity of graphene (Figure 2e, green circles) on the Ni substrate (Figure 2e, black circles). Inside the primary graphene spots, a series of satellite spots (Figure 2e, yellow circles) correspond to the 9.5 Å periodicity of the moiré unit cell. A rotation of 14.6° is determined by comparison with 1 × 1 graphene. The lower half of Figure 2c contains a more complex structure with no obvious moiré cell (see detail in Figure 2d). Taking the FFT of Figure 2d reveals the same primary spots attributable to graphene (Figure 2f, green circles), but the satellite features are markedly different. The chief difference is a set of square features indicating periodicities of 3.6 Å (Figure 2f, blue circles) and 5.2 Å (Figure 2f, purple circles)—proof that

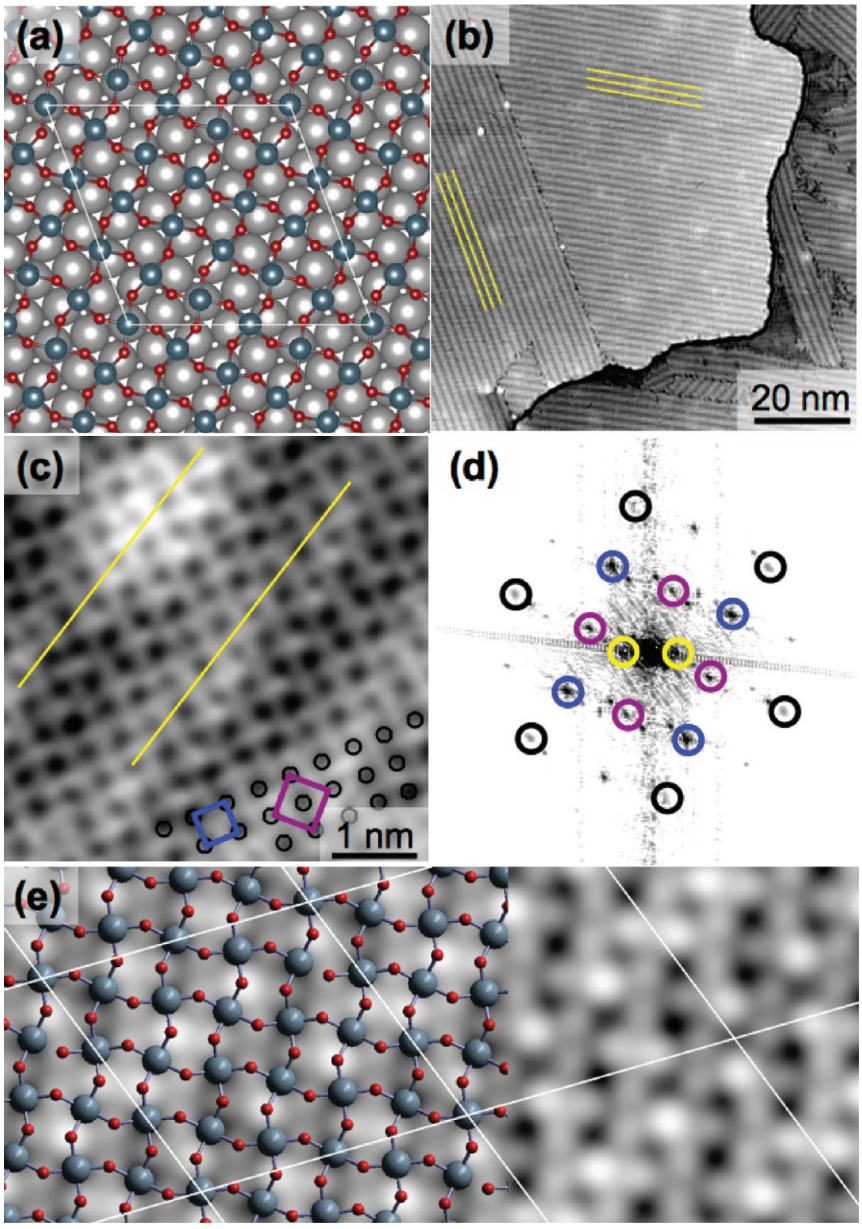

Figure 1. (a) Top view model of the ($\sqrt{39}R16.1° \times \sqrt{37}R$-34.7°) Ni_2C reconstruction (C, dark gray; surface Ni, red; bulk Ni, light gray) from DFT; white lines indicate the carbide unit cell. (b) Large-scale STM image of the Ni(111) surface covered with the Ni_2C reconstruction. The parallel stripes (marked in yellow) are indicative of Ni_2C. (c) High-resolution STM image of the Ni_2C surface. Black dots denote the position of individual carbon atoms. The yellow lines indicate the stripes observed in panel b. (d) FFT from the Ni_2C domain in panel c. Black circles correspond to the Ni(111) substrate; purple and blue circles highlight the nonhexagonal Ni_2C reconstruction; yellow circles indicate the stripes in panel b. (e) Simulated STM of Ni_2C overlaid with the model (C, dark gray; Ni, red).

graphene is adsorbed on Ni_2C and not Ni(111). We have observed graphene with rotations of 6.6, 9.8, 12.2, 14.6, 16.6, 19.1, 21.8, and 23.8° on or adjacent to Ni_2C patches. The appearance of rotated graphene on Ni_2C also depends on the orientation of the Ni_2C domain. Several examples are presented in the Supporting Information along with a simulated STM image (Figures S1−S4).

Figure 3a shows a rotated graphene grain embedded in a 1 × 1 graphene sheet. Depressions and bubbles are found throughout the rotated grain and at the grain boundary where 1 × 1 graphene meets the rotated graphene; a Ni_2C domain covered by graphene is circled in black. Figure 3b shows a tilt grain boundary and 1 × 1 grain boundary from the area outlined with a white box in Figure 3a. Aside from the grain boundaries and the rotated graphene, Figure 3b contains two hexagonal pits next to the tilt grain boundary; the graphene sheet is continuous over these features and does not expose the underlying Ni(111) surface. Figure 3c,d contains the FFTs from the 1 × 1 and rotated region in Figure 3b, respectively. In each FFT,

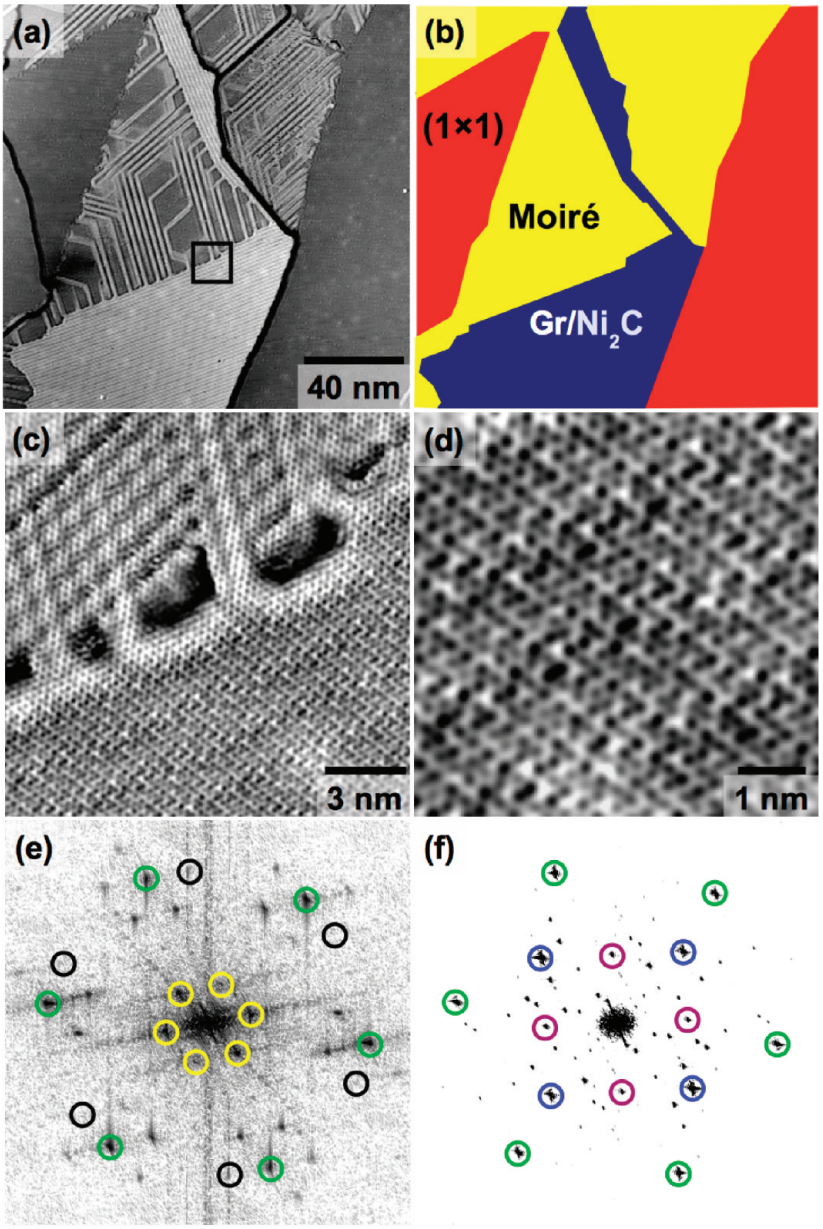

Figure 2. (a) Morphology of graphene grown on the surface in Figure 1b (illuminated from the left). Three distinct regions are found in this image and are marked in panel b for clarity. (b) Red indicates 1 × 1 epitaxial graphene on Ni(111); yellow represents graphene rotated away from 1 × 1 epitaxy; blue marks graphene residing on Ni_2C. (c) Zoom in on the boundary, marked with a black box in panel a. (d) Graphene adsorbed on the Ni_2C reconstruction (blue in panel b). (e) FFT of the upper half of panel c; green circles indicate the graphene lattice, black circles indicate the Ni(111) substrate, and yellow circles indicate the moiré unit cell. (f) FFT from the lower half of panel c; green circles indicate the graphene lattice, while purple and blue are nonhexagonal elements. The nonhexagonal features are the same as observed in Figure 1c.

the graphene lattice is indicated with green circles and Ni(111) with black circles. The rotated region has a moiré unit cell with a periodicity of 6 Å, which corresponds to a rotation of 23.8° (larger than found in Figure 2c). Figure 3e shows two line profiles taken over the hexagonal features in Figure 3b. The red line profile shows an initial decrease in the apparent height of 1.5 Å, followed by a further dip to 2.5 Å below the graphene surface. The blue line profile shows a different behavior by initially bulging away from the surface, then dropping sharply by 2 Å. As the interplane distance on Ni(111) is 2 Å, these line profiles indicate that nickel has been removed from under the graphene sheet. For the red line profile, two nickel layers have been removed or partially removed because the step is greater than 2 Å. The blue line profile indicates removal of one nickel layer.

We have used DFT calculations to gain additional insight on the stability of Ni_2C. Figure 4 gives an overview of the calculated free surface energies of Ni(111), the surface carbide Ni_2C/Ni(111), graphene/Ni(111), and graphene/Ni_2C/Ni(111) using LDA. At the

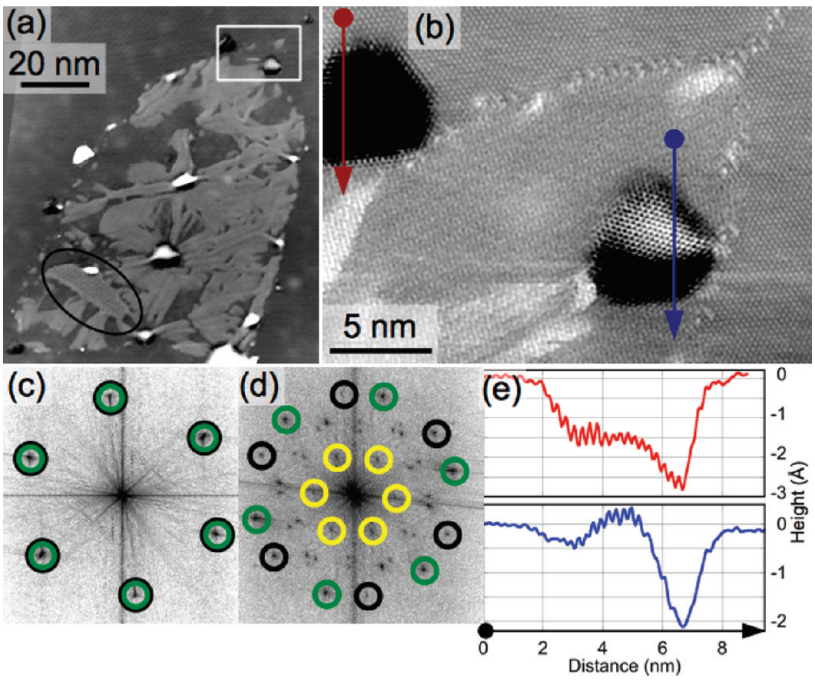

Figure 3. (a) Rotated graphene grain surrounded by 1 × 1 graphene. Inside the central region, a small domain of Ni_2C is circled in black. Bubbles, hexagonal depressions, and ripples are found in the central region. (b) Two types of grain boundaries are present in this image, a high angle tilt boundary between the rotated grain and the 1 × 1 graphene and a grain boundary between two 1 × 1 graphene domains (top right). Two hexagonal features are present at the tilt grain boundary. (c) FFT of the 1 × 1 graphene, excluding the hexagonal areas at the grain boundaries; green and black circles mark the graphene features and Ni(111), respectively. (d) FFT of the rotated grain; the green circles mark the rotated graphene, black circles mark the Ni(111) substrate, and yellow circles show the moiré unit of the rotated region. (e) Line profiles taken from panel b over the hexagonal features show the removal of nickel below the graphene sheet.

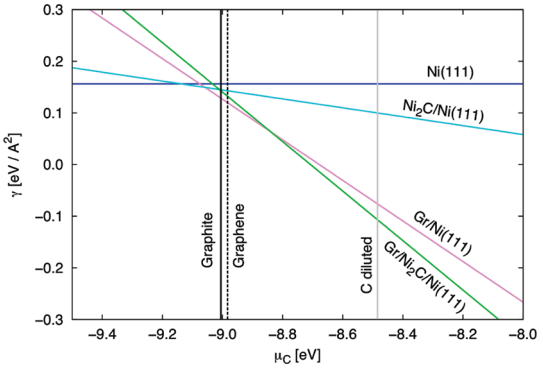

Figure 4. Free surface energies (LDA) of Ni(111), graphene/Ni(111), Ni_2C/Ni(111), and graphene/Ni_2C/Ni(111). The vertical lines indicate the specific value of the carbon chemical potential for graphite, graphene, and dissolved carbon; the chemical potential scale is referenced to a single carbon atom. The thermodynamically stable surface termination is given by the lowest energy line (entropy effects are neglected).

chemical potential of graphite ($\mu = -9.00$ eV), the LDA calculations predict a small decrease in the surface energy of 0.014 eV/Å^2 after the formation of Ni_2C and a further decrease upon the formation of a graphene layer on Ni(111). The choice of graphite as a reference for the chemical potential determines the respective thermodynamic stability *after* the dosing of hydrocarbons, while the relevant chemical potential of carbon can be significantly higher under growth conditions.[25−27] However, LDA predicts a binding energy that is too strong for graphene/Ni(111).[28] For this reason, we have also used the van der Waals density functional (vdw-DF), which was recently shown to reproduce more computationally expensive random phase approximation (RPA) calculations for the graphene/Ni(111) system.[28] The vdW-DF calculations predict a decreased stability (*i.e.*, higher surface energy) for the Ni_2C, making the surface carbide thermodynamically only metastable (see Supporting Information, Figure S5, light blue line). Nevertheless, at the chemical potential of graphite, both functionals predict a similar energy gain for the formation a graphene layer on Ni(111) from the Ni_2C surface carbide, as the surface energy is reduced by ∼20 meV/Å^2 for both functionals.

DISCUSSION

We have observed the coexistence of rotated graphene grains, interfacial nickel carbide, and nickel vacancy islands. To unravel the relationships between these features, we must examine the basic steps in the nickel carbide and graphene formation processes.

When clean nickel is exposed to hydrocarbons (*e.g.*, toluene) at 650 °C, the hydrocarbon is decomposed, allowing atomic carbon to dissolve into the nickel bulk. The incorporation of carbon into nickel at an optimized volume results in an increase of the total energy by

0.44 eV (LDA) and 0.71 eV (vdW-DF) per C atom (values at $T = 0$ K; with respect to phase separation into pure Ni and graphite). When sufficient carbon enters the bulk, the carbon–nickel solid solution reaches supersaturation and graphene nucleation can begin. Experimental evidence for this carbon–nickel solid solution comes from a diverse range of experimental techniques. Li *et al.* exposed Ni to alternating pressures of isotopically labeled methane during CVD growth and observed a mixture of Raman modes from each isotope using Raman microscopy.[29] This result implies diffusion of carbon into nickel followed by isotopic scrambling before graphene formation. X-ray photoelectron spectroscopy (XPS) has been used to watch the graphene formation process and identify the carbon chemical state during growth. By monitoring the C1s level, Grüneis *et al.* determined that graphene formation occurs at high temperature on a Ni(111) thin film and that Ni_2C is not directly transformed into graphene.[30] A low binding energy C1s feature was observed and attributed to hydrocarbon fragments but, in light of our results, may correspond to Ni_2C. A more recent study by Weatherup *et al.* looked at graphene formation on polycrystalline nickel and nickel–gold alloys.[9] Weatherup *et al.* performed an XPS depth profile by varying the incident photon energy, allowing identification of the carbon chemical state at the nickel surface and bulk. This XPS depth profile proved crucial in identifying carbidic carbon near the surface and an interstitial/dissolved carbon in the subsurface. Appreciable amounts of carbidic carbon were only observed at the start of graphene growth on pure nickel, and this species disappeared before graphene nucleation. Additional X-ray diffraction measurements rule out the formation of the metastable bulk nickel carbide, Ni_3C, during growth.

Graphene grown on a surface containing Ni_2C has not been deliberately investigated before, but due to the relevance of Ni_2C in the methanation reaction, much is known about Ni_2C surfaces. An early Auger electron spectroscopy (AES) study by Gardin *et al.* followed the carbon KVV Auger line with increasing temperature and measured the decomposition of the interfacial nickel carbide and subsequent diffusion of carbon into the nickel bulk.[23] Later studies with XPS observed carbidic carbon at temperatures up to 697 °C.[31] The common theme in these studies is decomposition of Ni_2C and the subsequent diffusion of carbon into nickel at elevated temperatures. The crucial point is that Ni_2C can survive on nickel surfaces at elevated temperatures similar to that used for graphene growth in our experiments. Therefore, we believe that Ni_2C found on the cold sample was present when the graphene growth began.

Further evidence for the presence of Ni_2C at growth temperatures is found in the vacancy islands shown in Figure 3. The formation of these features can be understood by first considering the structure of Ni_2C. When hydrocarbons are exposed to the clean Ni(111) surface, or when the bulk has a sufficient reservoir of carbon, the surface reconstructs into the clock reconstruction shown in Figure 1. This reconstruction alters the Ni(111) surface layer into a quasi-square symmetry reminiscent of the Ni(100) surface with a $c(2 \times 2)$ structure of adsorbed carbon. To transform the (111) surface into a (100)-like surface requires a reduction of the surface nickel density by 12%. The driving force behind this transformation is surface stress induced by the adsorption and incorporation of carbon.[22] Because the formation of Ni_2C occurs at elevated temperatures and the diffusion barrier for Ni adatoms on Ni(111) is small (0.22 eV[32]), excess nickel can diffuse to step edges. When a carbide domain starts to dissolve at high temperature—by diffusion of C into the Ni bulk or through consumption of the C in the graphene growth—there is a local deficit of Ni compared to the initial clean Ni(111) terrace. Dissolution of Ni_2C after graphene formation will therefore result in vacancy islands, as observed in Figure 3. Mass transport was experimentally observed in a TEM by Helveg *et al.* during carbon nanofiber growth on a Ni nanoparticle.[33] The aspect ratio (length/width) of the Ni nanoparticle catalyzing the growth increased throughout the growth process, indicating substantial mass transport. DFT calculations performed in the aforementioned study indicate moderate diffusion barriers for Ni and C under the graphene sheet. A similar set of *in situ* TEM experiments coupled with XPS and X-ray diffraction by Rinaldi *et al.*[34] recently determined that dissolved carbon drives the formation of disordered carbon nanofibers. In our study, we observe vacancy islands and residual Ni_2C below rotated graphene grains, indicating that a local Ni_2C domain was present at the time of graphene growth but the carbon in Ni_2C has diffused (presumably) into the bulk.

On the basis of observations similar to those shown in Figure 2, Lahiri *et al.*[20] proposed a new graphene growth model assuming the in-plane transformation of Ni_2C into graphene at low temperatures (<460 °C). Their model is based on the similar rotation of the graphene moiré pattern with that of Ni_2C. We have observed very similar features in our work (see Figure 2), but using FFT analysis, we prove that graphene is adsorbed *on* Ni_2C. In both halves of Figure 2c, we observe the same orientation of the graphene sheet; the upper half shows only hexagonal symmetry elements, while the lower half shows hexagonal and square symmetry elements. Looking at the ripples in Figure 2c, we see that the graphene lattice merges onto the Ni_2C domain whereupon the graphene lattice is modulated in a nonperiodic manner. We also note that at the temperatures utilized for graphene growth in this study Ni_2C remains on the Ni(111) surface.[31]

In addition, XPS studies by Weatherup *et al.* indicate that carbide is not directly converted to graphene.[9] Consequently, we suggest that Lahiri *et al.* did not observe the direct transformation of Ni_2C into graphene. Rather, we propose they observed graphene on Ni_2C. The Supporting Information (Figure S8) contains a detailed analysis showing how we reached this conclusion.

The DFT (LDA) calculations show that with an adsorption energy of 0.022 eV/C atom (vdW-DF: 0.068 eV/C) the adhesion of graphene on Ni_2C is weak and driven by the van der Waals interaction. For comparison, the interaction of graphene with Ni(111)—usually seen as a "strong" interaction due to the hybridization of the graphene π states—results in an adsorption energy of 0.101 eV/C (vdw-DF: 0.062 eV/C).[18] Therefore, standard DFT (LDA) predicts that the adhesion of graphene on the Ni_2C is significantly weaker compared to the bare Ni(111) surface, and the energy gain can drive the dissolution of the carbide under the graphene. Although the vdW-DF calculations (with the optB88 functional) predict a similar binding energy of graphene on the Ni_2C and the bare Ni surface (almost the same as in bulk graphite), the adsorption energies show a strong dependency on the choice of the vdW-DF functional,[28] hindering a quantitative comparison. Nevertheless, the average (LDA) distance of 3.16 Å (vdW-DF: 3.23 Å) between the graphene and Ni_2C is significantly larger than the 2.21 Å distance for graphene on Ni(111), indicating only van der Waals bonding of graphene on Ni_2C. Graphene that nucleates on Ni_2C has no epitaxial match to the underlying Ni(111) substrate, and the weak interaction with the Ni_2C enables a wide range of grain rotations. Rotation angles of 16.1 and 25° would result from alignment of the graphene lattice with the sides of the Ni_2C superstructure cell. We also note that there is a rough matching between the carbon lattice of Ni_2C (4.86 Å) and the defect scattering ($\sqrt{3} \times \sqrt{3}$)*R*30° electronic superstructure[35] in graphene (4.2 Å), aligning these structures produces a 13° rotation.

Evaluation of the free surface energy for the graphene/Ni_2C/Ni(111) system at the chemical potential of graphite yields a value of 0.152 eV/Å^2 (vdW-DF) and 0.143 eV/Å^2 (LDA), which is about 14 meV/Å^2 higher than graphene/Ni(111). On the other hand, under carbon-rich conditions (*e.g.*, during the growth of the carbide), the phase diagram indicates a high stability of the graphene-covered surface carbide. Therefore, while the calculations predict the formation of a graphene-covered surface carbide in carbon-rich conditions, the surface carbide is transformed to graphene/Ni(111) due to the higher stability of the graphene sheet on the bare Ni(111) surface at a lower chemical potential. This is consistent with the experimental observation of the lower stability of the graphene-covered surface carbide.

As a final note, we would like to mention that the graphene/Ni_2C formation process on our bulk Ni(111) single crystal may differ for epitaxial Ni(111) thin films, such as Ni(111)/W(110). Our bulk single crystals can support a larger reservoir of dissolved bulk carbon compared to thin film systems, and this may account for the observation of graphene/Ni_2C structures on bulk single crystals but not in thin films.

CONCLUSIONS

In conclusion, we have observed rotated graphene grains on the Ni(111) surface by STM. These rotated grains are unexpected given the widely reported 1 × 1 epitaxial match between Ni(111) and graphene. We have identified the surface-confined Ni_2C phase as a source of grain rotation in epitaxial graphene on Ni(111). Ni_2C is only found below rotated graphene grains, and nickel vacancy islands are found within and at the periphery of rotated grains—a clear indicator of carbide dissolution. DFT calculations predict that the graphene/Ni_2C/Ni(111) phase is stable when the carbon chemical potential is determined by the dilute carbon reservoir and predict a transformation to the graphene/Ni(111) as the dilute carbon reservoir (*i.e.*, the Ni bulk) is depleted. Grain rotation is facilitated by the weak binding energy of graphene on Ni_2C, and calculations indicate that adsorption is dominated by the van der Waals interaction. With a clear source of graphene grain rotation identified, mitigation strategies can be developed to reduce influence of grain boundaries on the properties of CVD-grown graphene.

EXPERIMENTAL AND THEORETICAL METHODS

The Ni(111) sample was cleaned by standard sputter/anneal cycles (60 min, 3 μA on sample, 2 keV, argon; 10 min at 600 °C). Graphene was grown by backfilling the chamber with toluene (C_7H_8, 1−3 × 10^{-6} mbar) while holding the Ni(111) crystal at 650 °C for 10 min. After growth, the chamber pressure recovered to the 10^{-9} mbar range within 3 min, and the sample reached ~80 °C in 15 min. We have also performed experiments where a hot sample (~400 °C) was transferred to a sample carousel after CVD growth for faster cooling to room temperature; no morphological changes were observed after this procedure. After repeated CVD cycles (~10 growths), the surface was found to contain nickel carbide after ~3 cleaning cycles. The surface carbide could be removed after extended cleaning (~30 cycles) or by sputtering while repeatedly ramping the sample temperature. We did not observe multilayer graphene on our samples, and STM and XPS results (Figure S7) are consistent with monolayer graphene. Scanning tunneling microscopy measurements were performed with an Omicron UHV-STM-1 in the same chamber used for sample preparation and graphene growth (base pressure 5 × 10^{-11} mbar). All STM measurements were performed in constant current mode with electrochemically etched W tips. For analysis of the fast Fourier transforms (FFT) of STM images, care has been taken to remove

image distortion, assuming that the Ni(111)(1 × 1) lattice remains undistorted. FFT maps are shown with logarithmic grayscale.

Spin-polarized DFT calculations were performed with the Vienna Ab initio Simulations Package (VASP),[36,37] using PAW potentials.[38] As standard generalized gradient approximation (GGA) potentials predict an endothermic adsorption of graphene on Ni(111) due to the neglect of the van der Waals contributions,[28] the calculations were performed on the basis of the vdW-DF[28] using the optB88 exchange correlation functional,[39] which offers a good description of the interaction of graphene and Ni,[28] and in the local density approximation (LDA).[40] The energy cutoff employed for both methods was 400 eV. The Ni lattice constant was optimized for the respective functional, 3.43 Å for LDA calculations and 3.51 Å for optB88 (which is close to the experimental lattice constant of 3.52 Å). The system was modeled with a ($\sqrt{39}R16.1° \times \sqrt{37}R\text{-}34.7°$) slab consisting of three supportive layers of Ni and a vacuum distance more than 10 Å. The geometry of the two bottom Ni layers was fixed. The graphene sheet was adsorbed on the Ni_2C surface in the orientation of the Ni(111) substrate leading to a slight deformation of the graphene sheet, which introduces an error of less than 0.008 (vdW-DF: 0.007) eV/C atom. A 2 × 2 × 1 k-point mesh was employed for the integration of the Brillouin zone. The formation energies of the diluted carbon were evaluated from a bulk cell of 32 Ni atoms both at a fixed volume (LDA: 0.52 eV, vdW-DF: 0.78 eV) and at an optimized volume (LDA: 0.44 eV, vdW-DF: 0.71 eV per C atom). All LDA structures were relaxed to forces lower than 0.02 eV/Å. The same geometries rescaled with the optB88 Ni bulk lattice constants were used for the vdw-DF calculations. We calculated the surface free energy γ in the *ab initio* thermodynamics framework as

$$\gamma(\mu_C) = (E_{tot} - N_{Ni}\mu_{Ni} - N_C(\mu_C + E_{Catom}))/A - E_{surf}(Ni(111))$$

where E_{tot} gives the total energy of the calculations, the chemical potential μ_{Ni} was set to the binding energy of bulk Ni, and the energy E_{Catom} of a single C atom was used as a reference value for carbon. The area of the surface unit cell is A, and the surface energy of a bare Ni(111) surface has been subtracted due to the bare Ni(111) surface at the back side of the slab geometry used in the calculations.

Conflict of Interest: The authors declare no competing financial interest.

Acknowledgment. This work was funded by Intel Corp. and the Austrian Science Fund (FWF) within the Wissenschaftskolleg WK04 and Grant I422-N16. The Vienna Scientific Cluster (VSC) is acknowledged for CPU time.

Supporting Information Available: Additional STM images and analysis of the graphene/Ni_2C/Ni(111) system, simulated STM image of graphene/Ni_2C/Ni(111), surface phase diagram using the optB88 functional, XPS spectra, LEED images, and an FFT analysis of the carbide structure observed in ref 20. This material is available free of charge *via* the Internet at http://pubs.acs.org.

REFERENCES AND NOTES

1. Geim, A. Graphene: Status and Prospects. *Science* **2009**, *324*, 1530.
2. Loh, K. P.; Bao, Q.; Eda, G.; Chhowalla, M. Graphene Oxide as a Chemically Tunable Platform for Optical Applications. *Nat. Chem.* **2010**, *2*, 1015–1024.
3. Stankovich, S.; Dikin, D. A.; Dommett, G. H. B.; Kohlhaas, K. M.; Zimney, E. J.; Stach, E. A.; Piner, R. D.; Nguyen, S. T.; Ruoff, R. S. Graphene-Based Composite Materials. *Nature* **2006**, *442*, 282–286.
4. Hass, J.; de Heer, W.; Conrad, E. The Growth and Morphology of Epitaxial Multilayer Graphene. *J. Phys.: Condens. Matter* **2008**, *20*, 323202.
5. Bostwick, A.; Mcchesney, J.; Ohta, T.; Rotenberg, E.; Seyller, T.; Horn, K. Experimental Studies of the Electronic Structure of Graphene. *Prog. Surf. Sci.* **2009**, *84*, 380–413.
6. Reina, A.; Jia, X.; Ho, J.; Nezich, D.; Son, H.; Bulovic, V.; Dresselhaus, M. S.; Kong, J. Large Area, Few-Layer Graphene Films on Arbitrary Substrates by Chemical Vapor Deposition. *Nano Lett.* **2008**, *9*, 30–35.
7. Li, X.; Cai, W.; An, J.; Kim, S.; Nah, J.; Yang, D.; Piner, R.; Velamakanni, A.; Jung, I.; Tutuc, E.; *et al.* Large-Area Synthesis of High-Quality and Uniform Graphene Films on Copper Foils. *Science* **2009**, *324*, 1312.
8. Wintterlin, J.; Bocquet, M. Graphene on Metal Surfaces. *Surf. Sci.* **2009**, *603*, 1841.
9. Weatherup, R.; Bayer, B.; Blume, R.; Ducati, C.; Baehtz, C.; Schlögl, R.; Hofmann, S. *In Situ* Characterization of Alloy Catalysts for Low-Temperature Graphene Growth. *Nano Lett.* **2011**, *11*, 4154–4160.
10. Lahiri, J.; S Miller, T.; J Ross, A.; Adamska, L.; Oleynik, I. I.; Batzill, M. Graphene Growth and Stability at Nickel Surfaces. *New J. Phys.* **2011**, *13*, 025001.
11. Chen, S.; Brown, L.; Levendorf, M. P.; Cai, W.; Ju, S.-Y.; Edgeworth, J.; Li, X.; Magnuson, C.; Velamakanni, A.; Piner, R.; *et al.* Oxidation Resistance of Graphene-Coated Cu and Cu/Ni Alloy. *ACS Nano* **2011**, *5*, 1321–1327.
12. Dai, B.; Fu, L.; Zou, Z.; Wang, M.; Xu, H.; Wang, S.; Liu, Z. Rational Design of a Binary Metal Alloy for Chemical Vapour Deposition Growth of Uniform Single-Layer Graphene. *Nat. Commun.* **2011**, *2*, 522.
13. Huang, P. Y.; Ruiz-Vargas, C. S.; Van Der Zande, A. M.; Whitney, W. S.; Levendorf, M. P.; Kevek, J. W.; Garg, S.; Alden, J. S.; Hustedt, C. J.; Zhu, Y.; *et al.* Grains and Grain Boundaries in Single-Layer Graphene Atomic Patchwork Quilts. *Nature* **2011**, *469*, 389–392.
14. Kim, K.; Lee, Z.; Regan, W.; Kisielowski, C.; Crommie, M.; Zettl, A. Grain Boundary Mapping in Polycrystalline Graphene. *ACS Nano* **2011**, *5*, 2142–2146.
15. Yu, Q.; Jauregui, L. A.; Wu, W.; Colby, R.; Tian, J.; Su, Z.; Cao, H.; Liu, Z.; Pandey, D.; Wei, D.; *et al.* Control and Characterization of Individual Grains and Grain Boundaries in Graphene Grown by Chemical Vapour Deposition. *Nat. Mater.* **2011**, *10*, 443–449.
16. Gao, L.; Guest, J. R.; Guisinger, N. P. Epitaxial Graphene on Cu(111). *Nano Lett.* **2010**, *10*, 3512–3516.
17. Zhao, W.; Kozlov, S. M.; Höfert, O.; Gotterbarm, K.; Lorenz, M. P.; Viñes, F.; Papp, C.; Görling, A.; Steinrück, H. P. Graphene on Ni(111): Coexistence of Different Surface Structures. *J. Phys. Chem. Lett.* **2011**, *2*, 759–764.
18. Lahiri, J.; Lin, Y.; Bozkurt, P.; Oleynik, I. I.; Batzill, M. An Extended Defect in Graphene as a Metallic Wire. *Nat. Nanotechnol.* **2010**, *5*, 326–329.
19. Dedkov, Y. S.; Fonin, M. Electronic and Magnetic Properties of the Graphene–Ferromagnet Interface. *New J. Phys.* **2010**, *12*, 125004.
20. Lahiri, J.; Miller, T.; Adamska, L.; Oleynik, I. I.; Batzill, M. Graphene Growth on Ni(111) by Transformation of a Surface Carbide. *Nano Lett.* **2010**, *10*, 1–5.
21. Murata, Y.; Petrova, V.; Kappes, B. B.; Ebnonnasir, A.; Petrov, I.; Xie, Y.-H.; Ciobanu, C. V.; Kodambaka, S. Moiré Superstructures of Graphene on Faceted Nickel Islands. *ACS Nano* **2010**, *4*, 6509–6514.
22. Klink, C.; Stensgaard, I.; Besenbacher, F.; Laegsgaard, E. An STM Study of Carbon-Induced Structures on Ni(111): Evidence for a Carbidic-Phase Clock Reconstruction. *Surf. Sci.* **1995**, *342*, 250–260.
23. Gardin, D. E.; Batteas, J. D.; Van Hove, M. A.; Somorjai, G. A. Carbon, Nitrogen, and Sulfur on Ni(111): Formation of Complex Structures and Consequences for Molecular Decomposition. *Surf. Sci.* **1993**, *296*, 25–35.
24. McCarroll, J.; Edmonds, T.; Pitkethly, R. Interpretation of a Complex Low Energy Electron Diffraction Pattern: Carbonaceous and Sulphur-Containing Structures on Ni(111). *Nature* **1969**, *223*, 1260–1262.
25. Teschner, D.; Révay, Z.; Borsodi, J.; Hävecker, M.; Knop-Gericke, A.; Schlögl, R.; Milroy, D.; Jackson, S. D.; Torres, D.; Sautet, P. Understanding Palladium Hydrogenation Catalysts: When the Nature of the Reactive Molecule Controls the Nature of the Catalyst Active Phase. *Angew. Chem., Int. Ed.* **2008**, *47*, 9274–9278.
26. Sautet, P.; Cinquini, F. Surface of Metallic Catalysts under a Pressure of Hydrocarbon Molecules: Metal or Carbide? *ChemCatChem* **2010**, *2*, 636–639.

27. Seriani, N.; Mittendorfer, F.; Kresse, G. Carbon in Palladium Catalysts: A Metastable Carbide. *J. Chem. Phys.* **2010**, *132*, 024711.
28. Mittendorfer, F.; Garhofer, A.; Redinger, J.; Klimeš, J.; Harl, J.; Kresse, G. Graphene on Ni(111): Strong Interaction and Weak Adsorption. *Phys. Rev. B* **2011**, *84*, 201401.
29. Li, X.; Cai, W.; Colombo, L.; Ruoff, R. Evolution of Graphene Growth on Ni and Cu by Carbon Isotope Labeling. *Nano Lett.* **2009**, *9*, 4268–4272.
30. Grüneis, A.; Kummer, K.; Vyalikh, D. Dynamics of Graphene Growth on a Metal Surface: A Time-Dependent Photoemission Study. *New J. Phys.* **2009**, *11*, 073050.
31. Wiltner, A.; Linsmeier, C. Thermally Induced Reaction and Diffusion of Carbon Films on Ni(111) and Ni(100). *Surf. Sci.* **2008**, *602*, 3623–3631.
32. Fu, T. Y.; Tsong, T. T. Atomic Processes in Self-Diffusion of Ni Surfaces. *Surf. Sci.* **2000**, *454−456*, 571–574.
33. Helveg, S.; Lopez-Cartes, C.; Sehested, J.; Hansen, P. L.; Cluasen, B. S.; Rostrup-Nielsen, J. R.; Abild-Pedersen, F.; Norskov, J. Atomic-Scale Imaging of Carbon Nanofibre Growth. *Nature* **2004**, *427*, 426–429.
34. Rinaldi, A.; Tessonnier, J.-P.; Schuster, M. E.; Blume, R.; Girgsdies, F.; Zhang, Q.; Jacob, T.; Abd Hamid, S. B.; Su, D. S.; Schlögl, R. Dissolved Carbon Controls the Initial Stages of Nanocarbon Growth. *Angew. Chem., Int. Ed.* **2011**, *50*, 3313–3317.
35. Ruffieux, P.; Melle-Franco, M.; Gröning, O.; Bielmann, M.; Zerbetto, F.; Gröning, P. Charge-Density Oscillation on Graphite Induced by the Interference of Electron Waves. *Phys. Rev. B* **2005**, *71*, 153403.
36. Kresse, G.; Hafner, J. *Ab Initio* Molecular Dynamics for Liquid Metals. *Phys. Rev. B* **1993**, *47*, 558.
37. Kresse, G.; Furthmüller, J. Efficiency of *Ab-Initio* Total Energy Calculations for Metals and Semiconductors Using a Plane-Wave Basis Set. *Comput. Mater. Sci.* **1996**, *6*, 15–50.
38. Blöchl, P. E. Projector Augmented-Wave Method. *Phys. Rev. B* **1994**, *50*, 17953.
39. Klimeš, J.; Bowler, D. R.; Michaelides, A. Chemical Accuracy for the Van Der Waals Density Functional. *J. Phys.: Condens. Matter* **2009**, *22*, 022201.
40. Kohn, W.; Sham, L. J. Self-Consistent Equations Including Exchange and Correlation Effects. *Phys. Rev.* **1965**, *140*, A1133–A1138.